

AEROELASTIC TAILORING BASED ON VIRTUALLY-GENERATED ALLOWABLES AND HIGH ORDER FINITE ELEMENTS FOR IMPROVED COMPOSITE WING DESIGN

P. H. Cabral¹, A. P. do Prado¹, E. Carrera², A. Pagani², A. Racionero Sánchez-Majano² & M. Enea²

¹Embraer S.A., São José dos Campos, São Paulo, Brazil. ²Mul2 Lab, Politecnico di Torino, Turin, Italy.

Abstract

Based on high order finite elements, this work proposes the use of progressive failure analysis outcomes to conceive new strain allowable curves to be used in aeroelastic tailoring of innovative composite wing design. The new allowable curves are generated by simulating coupons whose layup sequence may not fulfil some of the standard design rules considered in aircraft design. This allows us to explore different stacking sequences whose experimental testing would be unaffordable for the industry.

Keywords: Virtual testing; Aeroelastic tailoring; Failure constraints; High-order models.

1. Introduction

In an aeroelastic tailoring framework, the main aim is minimising the mass of the aircraft while guaranteeing specific mechanical performance and respecting constraints imposed during the design phase of the aircraft. These limitations can be referred to as physical and manufacturing constraints, respectively. Some examples of the former are requirements on the flutter speed, buckling loads and failure index. On the other hand, manufacturing constraints might be related to the layup sequence in the case of composite components. A list gathering the most spread manufacturing constraints is available in the works by Silva et al. [1] and Irisarri et al. [2].

Regarding the physical constraints, flutter speed and buckling loads are typically calculated through simulations comprising the aircraft's Global Finite Element Model (GFEM). In the case of metallic components, the failure indices are written in terms of strain components. Each component or a well-known combination, such as Von Mises, is limited. Contrariwise, when considering composites, strains are constrained by evaluating the strain resultant angles at 0° , $\pm 45^{\circ}$ or 90° , and comparing them to their Angle Minus Longitudinal (AML) allowable for both tension and compression. This is a standard procedure in the industry, as explained by Feraboli [3].

Considering manufacturing constraints and AML strain-based failure criteria limit the design space to just a tiny region of lamination parameters [4] and, hence, a limited number of stacking sequences. Such limitations penalise the aircraft designs and make them heavier.

One possible solution to minimise the structural weight could be the relaxation of some manufacturing constraints. Thus, more layups could be considered during the design phase. As a side effect, additional experimental testing would be necessary to characterise the mechanical behaviour of the new stacking sequences. Increasing the number of tests to perform is something the industry cannot afford. Therefore, there is a need for virtual testing campaigns that will complement the already existing experimental tests.

Virtual tests are a relatively straightforward manner of individuating the mechanical behaviour of laminates. The engineer modifies the fibre angle orientation associated with the individual laminae and runs a progressive failure analysis. This work provides a methodology for virtual testing based on FE models derived within the Carrera Unified Formulation (CUF) [5] framework. CUF serves as

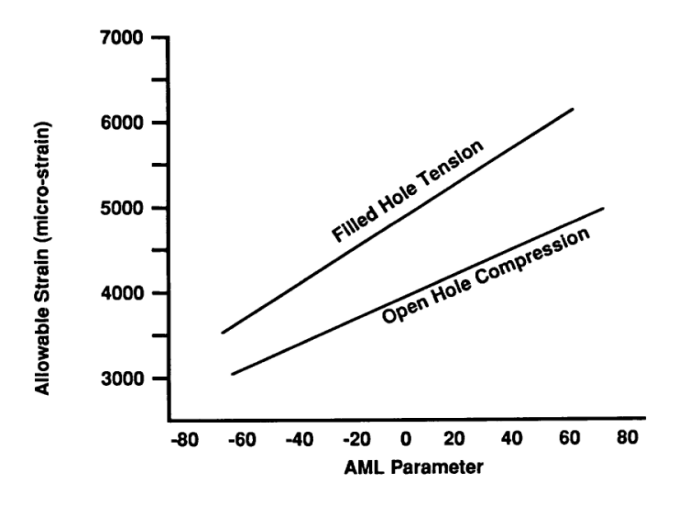


Figure 1 – Example of an AML versus strain allowable curve. Taken from [7].

a generator of structural theories for beam, plate and shell models and permits considering various theories of structures within the same analysis [6].

The document is organised as follows: First, the AML parameter is introduced, and the AML versus strain allowable curves are explained in Section 2. Then, CUF and the damage model are described in Section 3. Afterwards, the validation and application of the progressive failure analyses are discussed in Section 4. Finally, the concluding remarks are gathered in Section 5.

2. AML as an aeroelastic tailoring constraint

AML is a parameter that facilitates the characterisation of composite laminates [7]. It is computed as follows:

$$\mathsf{AML}[\%] = \frac{n_{\pm 45} - n_{load}}{n_{tot}} \cdot 100 \tag{1}$$

where $n_{\pm 45}$ is the number of layers oriented at $\pm 45^{\circ}$ with respect to the loading directions, n_{load} is the number of layers oriented in the loading direction, and n_{tot} is the total number of layers of the laminate.

The AML strain allowables are obtained by experimental testing for a fixed number of stacking sequence combinations. For instance, $[0,45,0,90,0,-45,0,45,0,-45]_s$, $[45,0,-45,90]_{2s}$ and $[\pm 45, 0, \pm 45, 90, \pm 45_2]_s$ laminates, which correspond to AML equal to -10%, 25% and 70%, respectively. The tests performed are un-notched tension (UNT) and compression (UNC), open-hole tension (OHT) and compression (OHC), and filled-hole tension (FHT) and compression (FHC) tests. Besides, different environmental operating conditions, material suppliers and curing cycle temperatures, among others, are considered during the experimental material characterisation. Subsequently, Aand B-basis statistics are computed to retrieve the strain allowable versus AML curves included as constraints in the aeroelastic tailoring framework. An example of these curves is available in Fig. 1. Further information regarding the generation of AML strain-based allowables can be found in [8]. Figure 2 illustrates how the design space is limited by applying the design rules depicted in [1, 2]. The unconstrained domain corresponds to the lamination parameter curve proposed by Fukunaga and Sekine [4]. Then, imposing a minimum AML percentage equal to -10%, and the 10% ply rule, the constrained design space corresponds to the inner rhomboid. The markers inside the rhomboid denote the different stacking sequences fulfilling the design rules. Each marker shape corresponds to a fixed number of layers in the layup.

3. Progressive failure modelling

3.1 Unified Formulation

The Carrera Unified Formulation (CUF) is employed in this work to generate high-order 2D FEs. According to [5], within the CUF framework the 3D displacement field of a plate can be expressed in terms of arbitrary through-the-thickness expansion functions, $F_{\tau}(z)$, of the generalized unknowns of

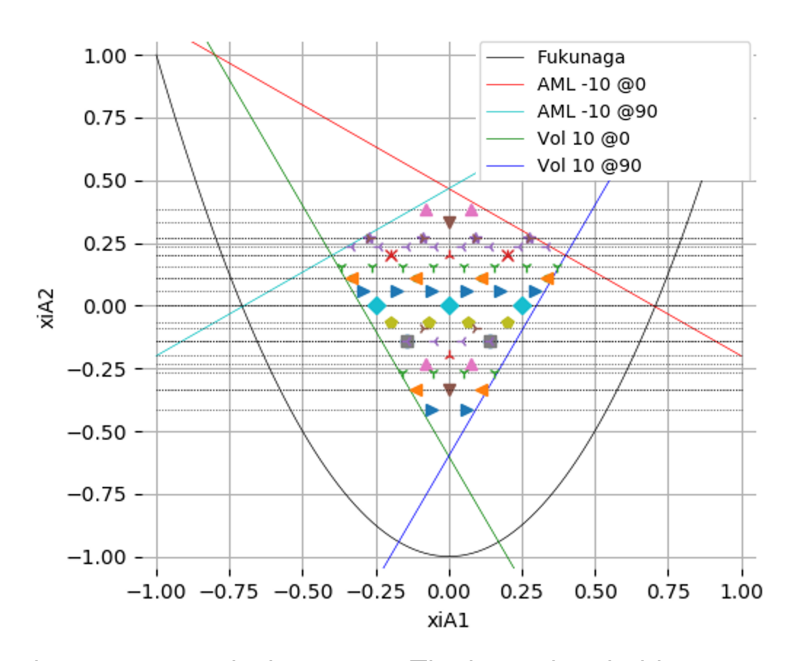


Figure 2 – Lamination parameter design space. The inner rhomboid corresponds to the design space after application of all the design rules.

the x - y plane. The equation can be written as follows:

$$\mathbf{u}(x,y,z) = F_{\tau}(z)\mathbf{u}_{\tau}(x,y), \qquad \tau = 1,\dots,M$$
 (2)

where M indicates the number of expansion terms and \mathbf{u}_{τ} the vector of the generalized displacements. The index τ means summation. The analysis of multi-layered structures is carried out by adopting a Layer-Wise (LW) approach [9]. It makes use of Lagrange polynomials as expansion functions over the single layers for the thickness direction, and then imposes the continuity of displacements at layer interfaces. The adoption of Lagrange Displacement-based (LD) expansion functions is indicated by the expression LDn, where a Lagrange polynomials of n-th order is used to describe each layer of the laminate.

A finite element formulation has been adopted within the CUF framework to solve the structural problem. The coupling of CUF formulation with FEM allows to deal with arbitrary geometry, loadings and boundary conditions. Independently of the adopted plate model kinematics, the FEM is used to discretize the generalized displacements vector \mathbf{u}_{τ} in the x-y plane as reported below:

$$\mathbf{u}_{\tau}(x,y) = N_i(x,y)\mathbf{q}_{\tau i}, \qquad i = 1,\dots,N_n$$
(3)

where N_i are the shape functions, $\mathbf{q}_{\tau i}$ denotes the unknown nodal variables, N_n stands for the number of nodes per element and the i indicates summation. Combining the FE approximation in Eq. 3 and CUF in Eq. 2, the 3D displacement field becomes:

$$\mathbf{u}(x, y, z) = F_{\tau}(z)N_i(x, y)\mathbf{q}_{\tau i}, \qquad \tau = 1, \dots, M \qquad i = 1, \dots, N_n$$

$$(4)$$

The derivation of the governing equations for the elasticity problem is made by means of the Principle of Virtual Displacements (PVD). According to PVD, for all kinematically admissible virtual displacements, a body is in equilibrium if the virtual work done by the internal stresses and inertial loads equals the work done by the external loads:

$$\delta L_{int} = \delta L_{ext} - \delta L_{ine} \tag{5}$$

where δL_{int} , δL_{ext} and δL_{ine} represent the virtual variation of the strain energy, the virtual variation of the work of external loads and the virtual variation of the inertia loads. In the case of linear static analysis, Eq. 5 reads:

$$\delta L_{int} = \delta L_{ext}$$
 (6)

AEROELASTIC TAILORING BASED ON VIRTUALLY-GENERATED ALLOWABLES FOR COMPOSITE WING DESIGN

The term related to the internal strain energy can be written as follows:

$$\delta L_{int} = \int_{V} \delta \boldsymbol{\varepsilon}^{\mathsf{T}} \boldsymbol{\sigma} \, dV \tag{7}$$

where V is the volume of the body. Equation 7 can be rewritten by using Eq. 3, the constitutive law and the geometrical relations between strains and displacement, leading to the following:

$$\delta L_{int} = \delta \mathbf{q}_{si} \mathbf{k}_{ii\tau s} \delta \mathbf{q}_{\tau i} \tag{8}$$

where $\mathbf{k}_{ij\tau s}$ is a 3×3 matrix called Fundamental Nucleus (FN) of the structural stiffness matrix. It should be noted that the formal expression of the FN remains invariable with respect to the structural theory or FE scheme chosen. Therefore, by simply looping on the indexes τ, i, j, s , any structural model can be created.

3.2 Damage model

This section describes the orthotropic damage model used in the current work, featured originally in [10, 11]. First, the constitutive relation for a damaged material is shown, including the definition of the damage variables. Then, the failure initiations are introduced in terms of failure criteria. Finally, the linear damage evolution law describing the failure progression of the independent crack modes is illustrated.

3.2.1 Stiffness formulation

The current orthotropic model deals with the assembly of the secant stiffness matrix in the damaged state \mathbf{C}^d , employed to compute the constitutive elastic stress-strain relation. By inverting the compliance matrix \mathbf{S}^d (Eq. 9), the stiffness matrix \mathbf{C}^d is then computed.

$$\mathbf{S}^{\mathsf{d}} = \begin{bmatrix} \frac{S_{11}}{1 - d_f} & S_{12} & S_{13} & 0 & 0 & 0\\ S_{21} & \frac{S_{22}}{1 - d_m} & S_{23} & 0 & 0 & 0\\ S_{31} & S_{32} & \frac{S_{33}}{1 - d_i} & 0 & 0 & 0\\ 0 & 0 & 0 & \frac{S_{44}}{1 - ds_{12}} & 0 & 0\\ 0 & 0 & 0 & 0 & \frac{S_{55}}{1 - ds_{13}} & 0\\ 0 & 0 & 0 & 0 & 0 & \frac{S_{66}}{1 - ds_{23}} \end{bmatrix}$$
(9)

With

$$S_{jj} = \frac{1}{E_{jj}}, \quad S_{jk} = S_{kj} = \frac{v_{jk}}{E_{jj}} = \frac{v_{kj}}{E_{kk}}, \quad j, k = 1, 2, 3, \quad j \neq k$$

$$S_{44} = G_{12}, \quad S_{55} = G_{13}, \quad S_{66} = G_{23}$$

$$(10)$$

The compliance matrix, assembled with the damage terms along the main diagonal, guarantees the consistency of the model and the thermodynamic admissibility [12]. The damage variables d_f , d_m , d_i refer to the fibre, matrix, and interlaminar failure modes, respectively, and both tensile and compressive behaviour are activated defining the relative effective stress $\hat{\sigma}_i$ [13]:

$$\hat{\sigma}_j = \frac{\sigma_j}{1 - d_j}, \qquad j = 1, 2, ..., 6$$
 (11)

With

$$d_{f} = d_{1} = \begin{cases} d_{ft} & \text{if } \hat{\sigma}_{1} \ge 0 \\ d_{fc} & \text{if } \hat{\sigma}_{1} \le 0 \end{cases}$$

$$d_{m} = d_{2} = \begin{cases} d_{mt} & \text{if } \hat{\sigma}_{2} \ge 0 \\ d_{mc} & \text{if } \hat{\sigma}_{2} \le 0 \end{cases}$$

$$d_{i} = d_{3} = \begin{cases} d_{it} & \text{if } \hat{\sigma}_{3} \le 0 \\ d_{ic} & \text{if } \hat{\sigma}_{3} \le 0 \end{cases}$$

$$(12)$$

The terms ds_{12} , ds_{13} and ds_{23} regulate the shear damage evolution, which depends on the fibre, matrix, and interlaminar damages, as stated in the following equation:

$$\begin{cases}
ds_{12} = d_4 = 1 - (1 - d_{ft})(1 - d_{fc})(1 - d_{mt})(1 - d_{mc}) \\
ds_{13} = d_5 = 1 - (1 - d_{ft})(1 - d_{fc})(1 - d_{it})(1 - d_{ic}) \\
ds_{23} = d_6 = 1 - (1 - d_{mt})(1 - d_{mc})(1 - d_{it})(1 - d_{ic})
\end{cases}$$
(13)

AEROELASTIC TAILORING BASED ON VIRTUALLY-GENERATED ALLOWABLES FOR COMPOSITE WING DESIGN

3.2.2 Failure onset and damage evolution

The onset of damage depends on the current stress field over the material. The damages involved in this framework include both tensile and compressive failure modes, and the simplifications adopted for the proposed model are described in [14] and [10]. The fibre damage initiation in the longitudinal direction occurs when the failure criterion $F_f = 1$, where:

$$F_{f} = \begin{cases} F_{ft} = \left(\frac{\hat{\sigma}_{1}}{X_{t}}\right)^{2} + \frac{\hat{\tau}_{12}^{2} + \hat{\tau}_{13}^{2}}{S_{L}^{2}}, & \text{if } \hat{\sigma}_{1} \ge 0\\ F_{fc} = \left(\frac{\hat{\sigma}_{1}}{X_{c}}\right)^{2}, & \text{if } \hat{\sigma}_{1} < 0 \end{cases}$$
(14)

 X_t and X_c represent the fibre tensile and compressive strengths, whereas S_L is the longitudinal shear strength. In the same manner, matrix F_m and interlaminar F_t failure criteria are defined,

$$F_{m} = \begin{cases} F_{mt} = \left(\frac{\hat{\sigma}_{2} + \hat{\sigma}_{3}}{Y_{t}}\right)^{2} + \frac{\hat{\tau}_{23}^{2} - \hat{\sigma}_{2}\hat{\sigma}_{3}}{S_{l}^{2}} + \frac{\hat{\tau}_{21}^{2} + \hat{\tau}_{31}^{2}}{S_{L}^{2}}, & \text{if } \hat{\sigma}_{2} + \hat{\sigma}_{3} \ge 0\\ F_{mc} = \left[\left(\frac{Y_{c}}{2S_{T}}\right)^{2} - 1\right] \left(\frac{\hat{\sigma}_{2} + \hat{\sigma}_{3}}{Y_{c}}\right) + \left(\frac{\hat{\sigma}_{2} + \hat{\sigma}_{3}}{2S_{T}}\right)^{2} + \frac{\hat{\tau}_{23}^{2} - \hat{\sigma}_{2}\hat{\sigma}_{3}}{S_{l}^{2}} + \frac{\hat{\tau}_{21}^{2} + \hat{\tau}_{31}^{2}}{S_{L}^{2}}, & \text{if } \hat{\sigma}_{2} + \hat{\sigma}_{3} < 0 \end{cases}$$
(15)

$$F_{i} = \begin{cases} F_{it} = \left(\frac{\hat{\sigma}_{3}}{Z_{t}}\right)^{2} + \left(\frac{\hat{\tau}_{31}}{S_{L}}\right)^{2} + \left(\frac{\hat{\tau}_{31}}{S_{I}}\right)^{2}, & \text{if } \hat{\sigma}_{3} \ge 0\\ F_{ic} = \left(\frac{\hat{\sigma}_{3}}{Z_{c}}\right)^{2}, & \text{if } \hat{\sigma}_{3} < 0 \end{cases}$$

$$(16)$$

 Y_t and Y_c are the matrix tensile and compressive strengths, Z_t and Z_c are the interlaminar tensile and compressive strengths, whereas S_T and S_I indicate the transversal and interlaminar shear strengths. According to [10], the computation of equivalent stress and strain is as follows:

$$\sigma_{eq}\varepsilon_{eq} = \sum \sigma_{ij}\varepsilon_{ij}, \quad \text{with} \quad \varepsilon_{eq} = \sqrt{\sum \varepsilon_{ij}^2}, \qquad i, j = 1, 2, ..., 6$$
 (17)

 ε_{eq} and σ_{eq} are the equivalent strain and stress consistent with [15],

$$\begin{cases} \varepsilon_{eq,ft} = \sqrt{\langle \varepsilon_{1} \rangle^{2} + \gamma_{12}^{2} + \gamma_{13}^{2}} \\ \varepsilon_{eq,fc} = \langle -\varepsilon_{1} \rangle \\ \varepsilon_{eq,mt} = \sqrt{\langle \varepsilon_{2} \rangle^{2} + \langle \varepsilon_{3} \rangle^{2} + \gamma_{21}^{2} + \gamma_{23}^{2} + \gamma_{31}^{2}} \\ \varepsilon_{eq,mc} = \sqrt{\langle -\varepsilon_{2} \rangle^{2} + \langle -\varepsilon_{3} \rangle^{2} + \gamma_{21}^{2} + \gamma_{23}^{2} + \gamma_{31}^{2}} \\ \varepsilon_{eq,ic} = \sqrt{\langle \varepsilon_{3} \rangle^{2} + \gamma_{31}^{2} + \gamma_{32}^{2}} \\ \varepsilon_{eq,ic} = \langle -\varepsilon_{3} \rangle \end{cases}$$

$$(18)$$

$$\begin{cases}
\sigma_{eq,ft} = \frac{\langle \sigma_{1} \rangle \langle \varepsilon_{1} \rangle + \tau_{12} \gamma_{12} + \tau_{13} \gamma_{13}}{\sqrt{\langle \varepsilon_{1} \rangle^{2} + \gamma_{12}^{2} + \gamma_{13}^{2}}} \\
\sigma_{eq,fc} = \langle -\sigma_{1} \rangle \\
\sigma_{eq,mt} = \frac{\langle \sigma_{2} \rangle \langle \varepsilon_{2} \rangle + \langle \sigma_{3} \rangle \langle \varepsilon_{3} \rangle + \tau_{21} \gamma_{21} + \tau_{23} \gamma_{23} + \tau_{31} \gamma_{31}}{\sqrt{\langle \varepsilon_{2} \rangle^{2} + \langle \varepsilon_{3} \rangle^{2} + \gamma_{21}^{2} + \gamma_{23}^{2} + \gamma_{31}^{2}}} \\
\sigma_{eq,mc} = \frac{\langle -\sigma_{2} \rangle \langle -\varepsilon_{2} \rangle + \langle -\sigma_{3} \rangle \langle -\varepsilon_{3} \rangle + \tau_{21} \gamma_{21} + \tau_{23} \gamma_{23} + \tau_{31} \gamma_{31}}{\sqrt{\langle -\varepsilon_{2} \rangle^{2} + \langle -\varepsilon_{3} \rangle^{2} + \gamma_{21}^{2} + \gamma_{23}^{2} + \gamma_{31}^{2}}} \\
\sigma_{eq,it} = \frac{\langle \sigma_{3} \rangle \langle \varepsilon_{3} \rangle + \tau_{31} \gamma_{31} + \tau_{32} \gamma_{32}}{\sqrt{\langle \varepsilon_{3} \rangle^{2} + \gamma_{31}^{2} + \gamma_{32}^{2}}} \\
\sigma_{eq,ic} = \langle -\sigma_{3} \rangle
\end{cases}$$
(19)

where $\langle \cdot \rangle$ denotes the Macaulay bracket. By solving the failure criteria defined in Eqs. 14, 15, and 16, the initial equivalent stress σ_{eq}^0 and strain ε_{eq}^0 are then retrieved. The calculation of equivalent stress and strain in the onset of damage is required to define the constitutive evolution law. In this work, the damage evolution follows a linear softening path, and the damage d in the post-peak branch is defined using the following equation:

$$d = \begin{cases} \frac{\delta_{eq}^{u}(\delta_{eq} - \delta_{eq}^{0})}{\delta_{eq}(\delta_{eq}^{u} - \delta_{eq}^{0})}, & \text{if } \delta_{eq}^{0} \le \delta_{eq} \le \delta_{eq}^{u} \\ 1, & \text{if } \delta_{eq} > \delta_{eq}^{u} \end{cases}$$
(20)

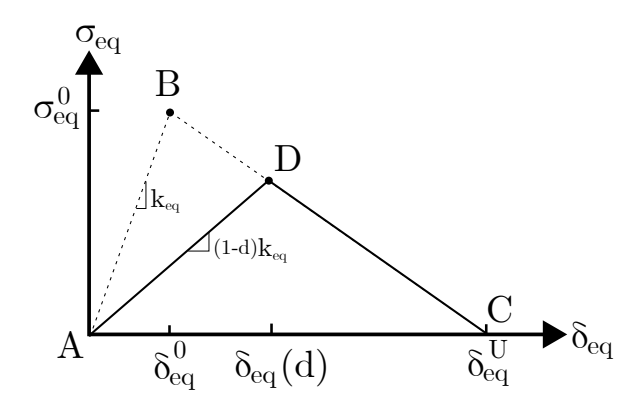


Figure 3 – Constitutive relation for the equivalent stress and displacement.

Table 1 – Material properties and strength characteristics used for the model validation analysis.

Material properties		Strength characteristics		
<i>E</i> ₁ [GPa]	139.0	X_T [MPa]	2170.0	
E_2 , E_3 [GPa]	10.0	X_C [MPa]	2013.2	
G_{12} , G_{13} [GPa]	5.2	Y_T , Z_T [MPa]	73.0	
G_{23} [GPa]	10.0	Y_C , Z_C [MPa]	400.35	
v_{12}, v_{13} [-]	0.32	S_L , S_T [MPa]	77.84	
v ₂₃ [-]	0.32	S_I [MPa]	77.84	

where δ_{eq} is the equivalent displacement, and δ^u_{eq} is considered as the equivalent displacement when the damage d=1.

$$\delta_{eq} = L_c \varepsilon_{eq}$$
 and $\delta^u_{eq} = \frac{2G_a}{\sigma_{eq}}$ (21)

 L_c stands for the characteristic length [16], used to reduce the mesh dependency. The current work considers $L_c = (V_{GP})^{\frac{1}{3}}$, where V_{GP} is the Gauss point volume of the given element, as previously done in [17, 18]. G_a represents the fracture energy of the independent damage mode a, corresponding to the area $A\hat{B}C \Rightarrow (\varepsilon_{eq}(d=0))$ under the curve of the linear evolution law, see Fig. 3.

4. Results

4.1 Progressive failure analyses

This section provides the numerical outcomes for the progressive failure analysis of laminated coupons. As of now, only OHT tests are replicated. The coupons follow the ASTM D5766 guidelines. Each coupon has a 300 mm length, 36 mm width, and a hole diameter equal to 6 mm. The numerical models use nine-node bi-guadratic FE and a linear through-the-thickness LD expansion.

4.1.1 Validation

The $[90,0]_{2s}$ coupon from [19] is used for the validation of the proposed numerical framework. Table 1 lists the material properties and strengths.

Figure 4 shows the stress-strain curve of the $[90,0]_{2s}$ specimen from the reference [19] and with the present progressive failure approach. A good agreement in predicting the strain at peak load is found. However, there is a mismatch in the expected peak load. It is due to eventual differences between the Young's modulus of the physical and virtual coupons. Despite the disagreement in the ultimate load, a remarkable prediction of strain failure point has been obtained. It is of utmost importance as the AML failure index curves provide allowable strains.

4.1.2 Virtual testing of multi-layered coupons

In this section, coupons comprising seven and eight layers are investigated. The material used is Hexcel IM7/8552, whose elastic properties and strengths are reported in Table 2. The stacking sequences of the studied coupons are available in Tables 3. Note that LAM 7.1 and 7.6 are the

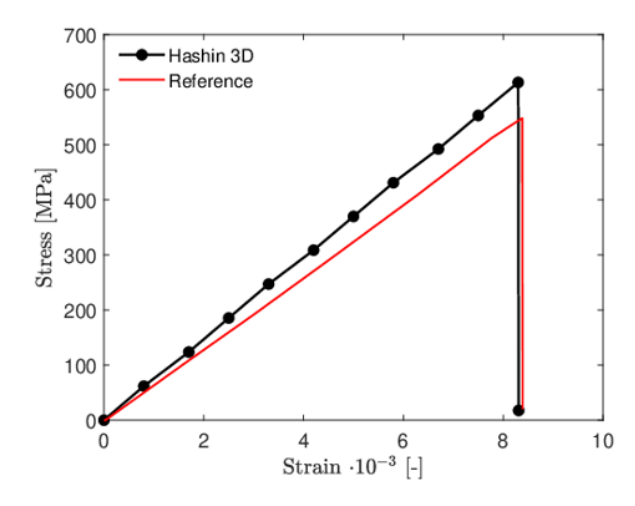


Figure 4 – Stress-strain curve of the $[90,0]_{2s}$ coupon used for validation.

Table 2 – Material properties and strength characteristics used for the seven- and eight-layered coupons analyses.

Material properties		Strength characteristics		
<i>E</i> ₁ [GPa]	152.0	X_T [MPa]	2438.0	
E_2 , E_3 [GPa]	9.3	X_C [MPa]	2013.2	
G_{12}, G_{13} [GPa]	4.7	Y_T, Z_T [MPa]	66.19	
G_{23} [GPa]	4.7	Y_C , Z_C [MPa]	381.35	
v_{12}, v_{13} [-]	0.27	S_L , S_T [MPa]	77.84	
<i>v</i> ₂₃ [-]	0.27	S_I [MPa]	77.84	

only ones that do not respect all the manufacturing constraints used. Indeed, they are unbalanced laminates since there is no equal number of 45° and -45° layers. They are considered to investigate how the strain curves may vary if some design rules are not fulfilled. The AML in the 0° direction, calculated through Eq. (1), is included in the tables.

The stress-strain curves of the eight-layered coupons are illustrated in Fig. 5. The six laminates show practically identical curves. They all fail at the same strain with a similar peak load value. Furthermore, the damage evolution around the coupon hole is illustrated in Fig. 6.

Figure 7 shows the strains at peak load of the seven- and eight-layered coupons. The experimental A- and B-basis strain allowable curves are also reported. Two additional curves are represented. They are traced using the virtual testing data. One corresponds to the strain lower bound of the coupons, respecting all the design rules. The other is the lower bound when unbalanced stacking sequences are considered.

From Fig. 7, it is inferred that A- and B-basis allowable are too conservative compared to the virtual testing curves. Indeed, a 131% and 25% relative difference in the strain allowable is observed between A- and B-basis with respect to the unbalanced lower bound. Of course, the unbalanced bound did not consider any uncertainty in the material properties, environmental operating conditions, or other factors implicit in the experimental allowables.

4.2 Aeroelastic tailoring

The new AML strain allowable curve, considering the unbalanced coupons, was included as a physical constraint in Embraer's aeroelastic tailoring methodology [1]. An FE model of Embraer's benchmark wing was considered for the application of the new constraint. The benchmark wing was design for a generic aircraft with requirements similar to those of the Embraer E-Jets family. The optimal solutions that used the experimental (B-basis) and CUF-based virtual testing allowable are compared. Table 4 shows the wing's initial mass and the mass after the optimisation processes. A 5% weight reduction is obtained with the virtual allowables. Figure 8 displays the history of the optimisation pro-

Table 3 – Stacking sequences of the seven- and eight-layered coupons.

	Identifier	AML ₀ [%]	Layup
	LAM 7.1	14.28	[90,-45,0,45,0,-45,90]
	LAM 7.2	28.57	[45,0,-45,90,-45,0,45]
Seven-layered	LAM 7.3	28.57	[-45,90,45,0,45,90,-45]
	LAM 7.4	28.57	[-45,0,45,90,45,0,-45]
	LAM 7.5	42.86	[45,90,-45,0,-45,90,45]
	LAM 7.6	14.28	[90,45,0,-45,0,45,90]
	LAM 8.1	25	[90,-45,0,45,45,0,-45,90]
Eight-layered	LAM 8.2	25	[45,0,-45,90,90,-45,0,45]
	LAM 8.3	25	[-45,90,45,0,0,45,90,-45]
	LAM 8.4	25	[-45,0,45,90,90,45,0,-45]
	LAM 8.5	25	[45,90,-45,0,0,-45,90,45]
	LAM 8.6	25	[90,45,0,-45,-45,0,45,90]

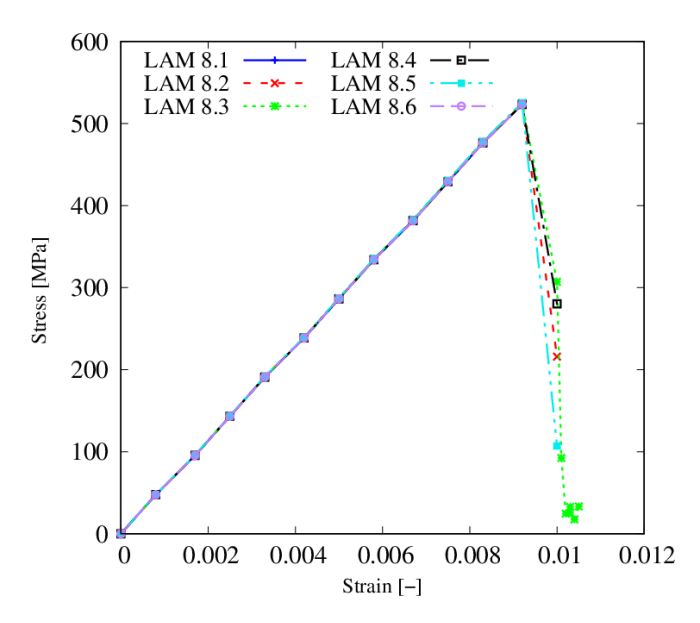


Figure 5 – Stress-strain curves of the eight-layered coupons.

Table 4 – Mass optimisation results using experimental and CUF-based allowables.

Initial mass [kg]	1621.75
Non structural mass [kg]	166.9
Total mass w/ Exp. Allowables [kg]	1386.4
Total mass w/ CUF OHT	1316.4
Total mass difference [kg]	-70.0
Total mass difference [%]	-5.0

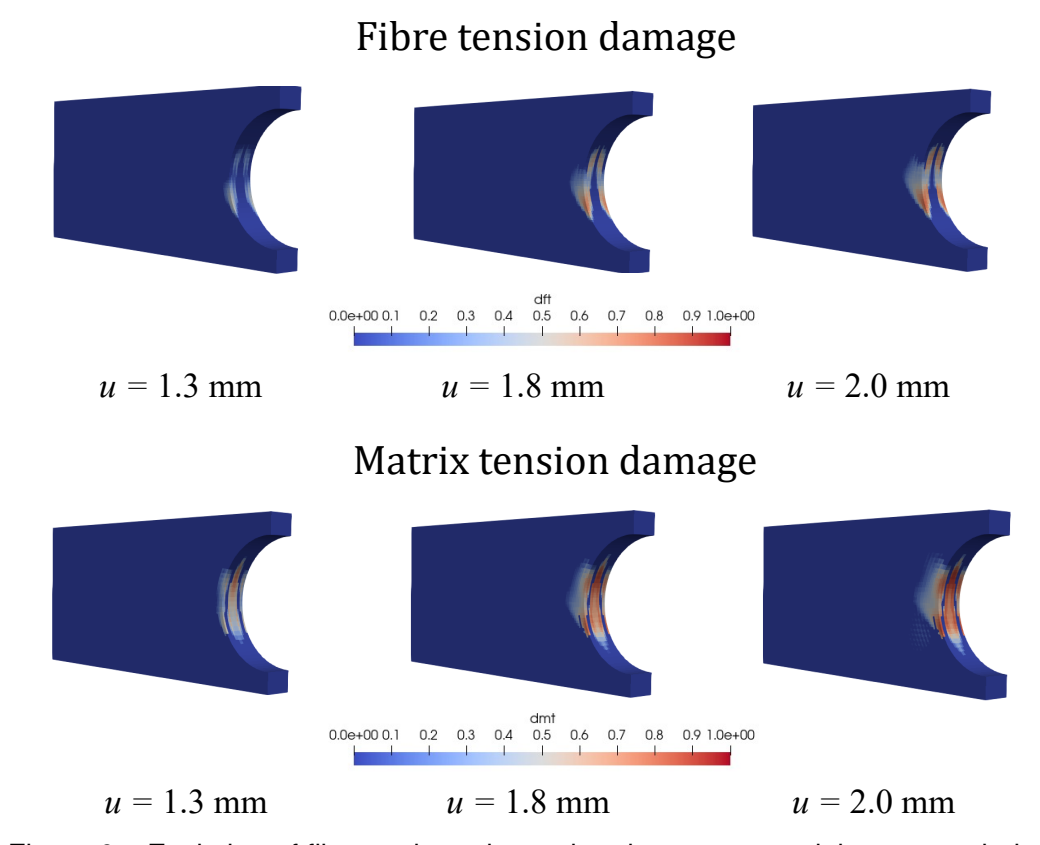


Figure 6 – Evolution of fibre and matrix tension damage around the coupon hole.

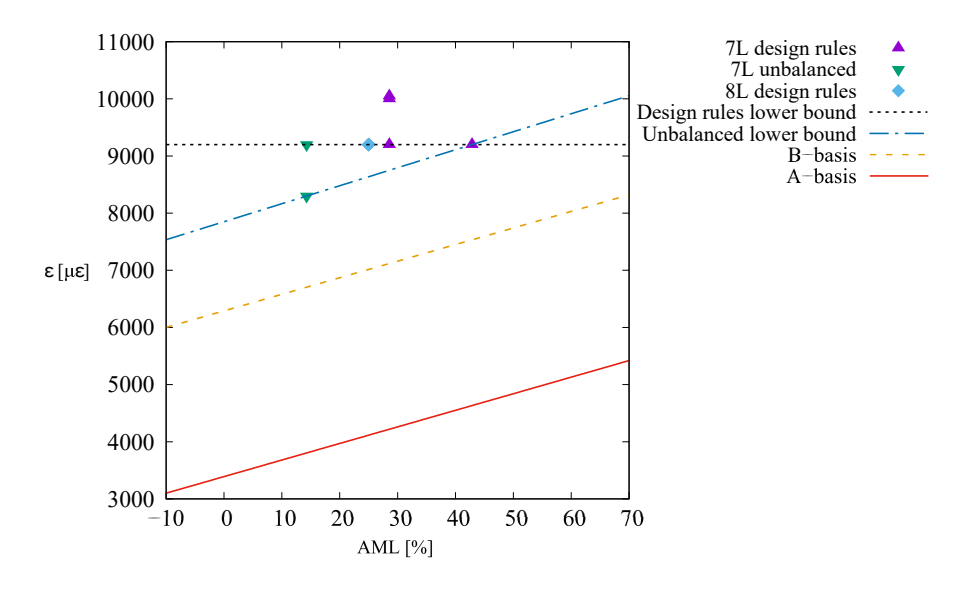


Figure 7 – Strain allowables versus AML curves obtained by virtual testing of seven- and eight-layered coupons.

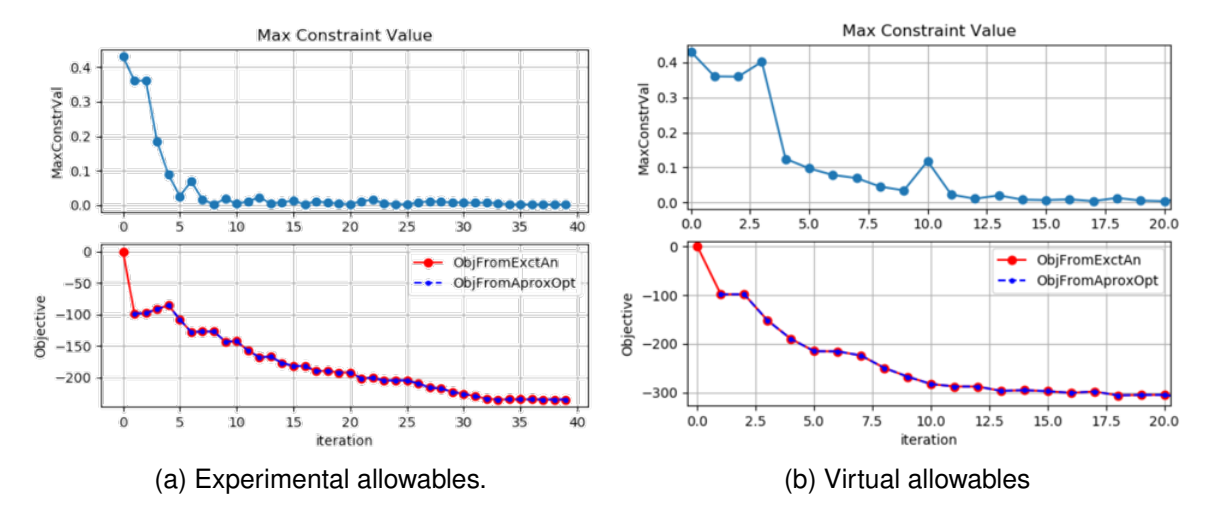


Figure 8 – Optimisation history using (a) experimental and (b) virtual allowables as physical constraint.

cess. It is observed that the virtual allowable results converge faster than the experimental allowables. This is due to the relaxation of the failure constraint. In addition, the local buckling modes occurring at the loading condition are illustrated in Fig. 9. Slight differences are observed. For instance, Fig. 9a presents some undulations at the leading and trailing edge at midspan, while in Fig.9b, these are present chord-wise. Last, failure constraints are reported in Fig. 10. The main discrepancies between the two optimised results are observed in the highlighted region, where cutouts are present, and in the right wing close to the engine pylon.

5. Conclusions

This document showed the validity of the present approach for virtual testing of laminated composite coupons. OHT tests were carried out, and the strains at coupon failure were used to build strain allowable curves. The input of those curves is the AML percentage of a laminate, which allows straightforwardly retrieving the ultimate strain.

After the validation of the presented CUF-based FE models, two sets of coupons were simulated. One of the sets, comprising seven- and eight-layered coupons, fulfilled all the design rules; the other set did not guarantee the balanced laminate condition. The virtual strain allowables had a similar order of magnitude as the experimental ones. The difference in the strain value is due to not considering the uncertainty associated with the manufacturing processes, working environmental conditions, and material suppliers, among others.

Later, the virtually generated curve was introduced as a constraint of the aeroelastic optimisation solver. A lighter wing design was retrieved. It satisfied the buckling and failure index constraints similarly to the optimal solution that used the experimental allowables as a constraint.

The main conclusions that can be drawn from this work are the following:

- Generating new allowable curves, combining physical and virtual tests, can help relax the failure index constraints during the aeroelastic optimisation and, thus, conceiving lighter aircraft.
- The tailoring design space can be enlarged by considering new stacking sequence combinations that do not necessarily fulfil the design rules imposed so far and whose testing cost would be unaffordable for the industry.

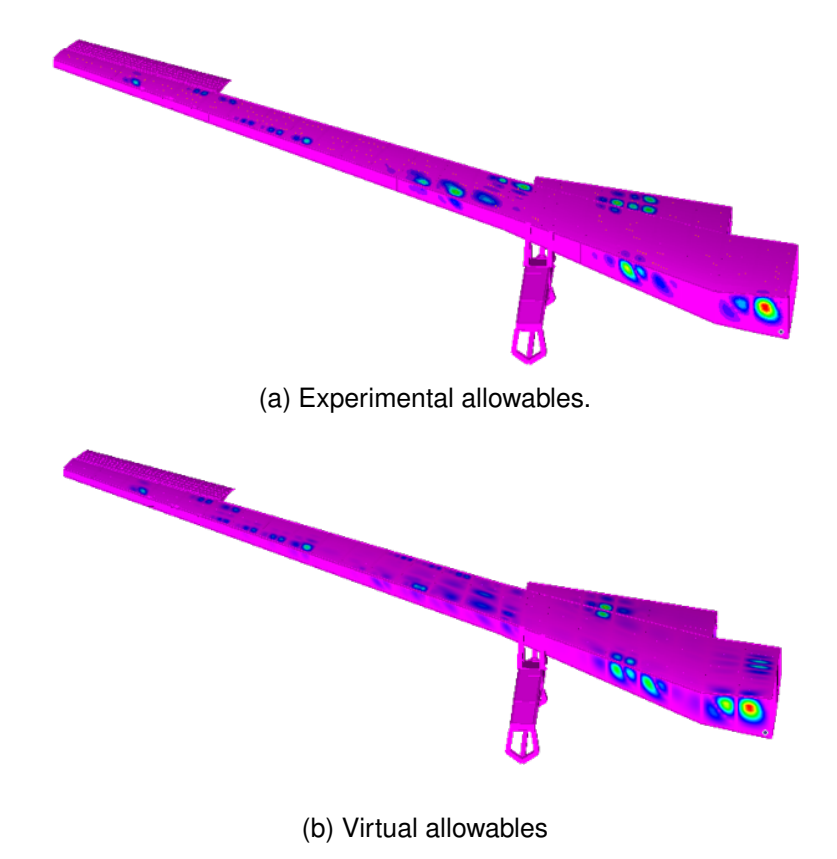


Figure 9 – Buckling constraint using (a) experimental and (b) virtual allowables as physical constraint.

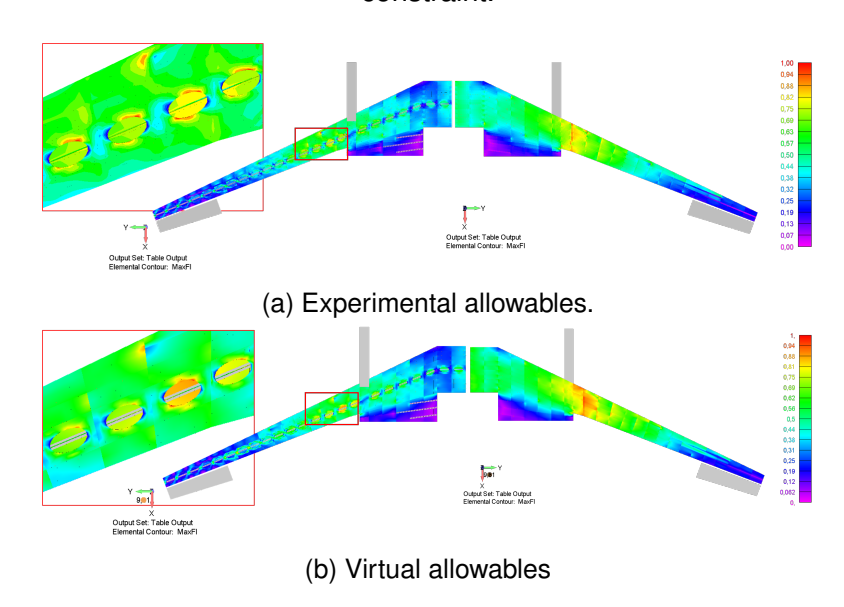


Figure 10 – Failure constraint using (a) experimental and (b) virtual allowables as physical constraint.

6. Contact Author Email Address

Inquiries regarding this paper should be sent to alfonso.pagani@polito.it.

7. Copyright Statement

The authors confirm that they, and/or their company or organization, hold copyright on all of the original material included in this paper. The authors also confirm that they have obtained permission, from the copyright holder of any third party material included in this paper, to publish it as part of their paper. The authors confirm that they give permission, or have obtained permission from the copyright holder of this paper, for the publication and distribution of this paper as part of the ICAS proceedings or as individual off-prints from the proceedings.

AEROELASTIC TAILORING BASED ON VIRTUALLY-GENERATED ALLOWABLES FOR COMPOSITE WING DESIGN

References

- [1] Silva, G. H. C., do Prado, A. P., Cabral, P. H., De Breuker, R., and Dillinger, J. K. S. Tailoring of a composite regional jet wing using the slice and swap method. *Journal of Aircraft*, 56(3):990–1004, 2019.
- [2] Irisarri, F. X., Lasseigne, A., Leroy, F. H., and Le Riche, R. Optimal design of laminated composite structures with ply drops using stacking sequence tables. *Composite Structures*, 107:559–569, 2014.
- [3] Feraboli, P. Composite materials strength determination within the current certification methodology for aircraft structures. *Journal of Aircraft*, 46(4):1365–1374, 2009.
- [4] Fukunaga, H. and Sekine, H. Stiffness design method of symmetric laminates using lamination parameters. *AIAA Journal*, 30(11):2791–2793, 1992.
- [5] Carrera, E., Cinefra, M., Petrolo, M., and Zappino, E. *Finite Element Analysis of Structures through Unified Formulation*. Wiley & Sons, Hoboken, New Jersey, USA, 2014.
- [6] Petrolo, M. and Iannotti, P. Best theory diagrams for laminated composite shells based on failure indexes. *Aerotecnica Missili & Spazio*, 102(3):199–218, 2023.
- [7] Dorris, W. J., Hairr, J. W., Huang, J. T., Ingram, J. E., and Shah, B. M. Advanced composites structural concepts and materials technologies for primary aircraft structures. structural response and failure analysis. Technical report, 1992.
- [8] Marlett, K., Yeow, Ng., and Tomblin, J. Hexcel 8552 IM7 unidirectional prepreg 190 gsm & 35% rc qualification material property data report. *National Center for Advanced Materials Performance, Wichita, Kansas. Test Report CAM-RP-2009-015, Rev. A*, pages 1–238, 2011.
- [9] Scano, D., Carrera, E., and Petrolo, M. Use of the 3d equilibrium equations in the free-edge analyses for laminated structures with the variable kinematics approach. *Aerotecnica Missili & Spazio*, pages 1–17, 2023.
- [10] Arruda, M. R. T., Trombini, M., and Pagani, A. Implicit to Explicit Algorithm for ABAQUS Standard User-Subroutine UMAT for a 3D Hashin-Based Orthotropic Damage Model. *Applied Sciences*, 13(2), 2023.
- [11] Trombini, M., Enea, M., Arruda, M. R. T., Pagani, A., Petrolo, M., and Carrera, E. 1D higher-order theories for quasi-static progressive failure analysis of composites based on a full 3d hashin orthotropic damage model. *Composites Part B: Engineering*, page 111120, 2023.
- [12] Matzenmiller, A. L. J. T. R., Lubliner, J., and Taylor, R. L. A constitutive model for anisotropic damage in fiber-composites. *Mechanics of materials*, 20(2):125–152, 1995.
- [13] Lemaitre, J. and Chaboche, J. L. *Mechanics of solid materials*. Cambridge university press, 1994.
- [14] Hashin, Z. Failure Criteria for Unidirectional Fiber Composites. *Journal of Applied Mechanics*, 47(2):329–334, 06 1980.
- [15] Lapczyk, I. and Hurtado, J. A. Progressive damage modeling in fiber-reinforced materials. *Composites Part A: Applied Science and Manufacturing*, 38(11):2333–2341, 2007.
- [16] Bazant, Z. and Oh, B. Crack Band Theory for Fracture of Concrete. *Matériaux et Constructions*, 16:155–177, 05 1983.
- [17] Kaleel, I., Petrolo, M., Waas, A. M., and Carrera, E. Micromechanical progressive failure analysis of fiber-reinforced composite using refined beam models. *Journal of Applied Mechanics*, 85(2):021004, 2018.
- [18] Nagaraj, M. H., Reiner, J., Vaziri, R., Carrera, E., and Petrolo, M. Progressive damage analysis of composite structures using higher-order layer-wise elements. *Composites Part B: Engineering*, 190:107921, 2020.
- [19] O'Higgins, R. M., McCarthy, M. A., and McCarthy, C. T. Comparison of open hole tension characteristics of high strength glass and carbon fibre-reinforced composite materials. *Composites Science and Technology*, 68(13):2770–2778, 2008.